LI, Y., PAN, D.Z., CHANSON, H., and PAN, C.H. (2019). "Real-Time Characteristics of Tidal Bore Propagation in the Qiantang River Estuary, China, Recorded by Marine Radar." *Continental Shelf Research*, Vol. 180, pp. 48-58 (DOI: 10.1016/j.csr.2019.04.012) (ISSN 0278-4343).

Real-Time Characteristics of Tidal Bore Propagation in the Qiantang River Estuary, China, Recorded by Marine Radar

Ying Li [1], Dong-Zi Pan [2,] *, Hubert Chanson[3] and Cun-Hong Pan [2]

[1] School of Surveying and municipal engineering, Zhejiang University of Water Resources and Electric Power, 583 Xuelin Street, Hangzhou 310018, China; liying@zjweu.edu.cn

[2] Zhejiang Institute of Hydraulics and Estuary, 50 East Fengqi Road, Hangzhou 310020, China; pandz@zjwater.gov.cn (D.P.); panch@zjwater.gov.cn (C.P.)

[3] The University of Queensland, School of Civil Engineering, Brisbane, QLD 4072, Australia; h.chanson@uq.edu.au

In preparation for *Continental Shelf Research*

*** Corresponding author:** Dong-Zi Pan, Zhejiang Institute of Hydraulics and Estuary, 50 East Fengqi Road, Hangzhou 310020, China. Email: pandz@zjwater.gov.cn; Tel.: +86-571-8643-8014.

Declarations of interest: none.

Abstract

Quantitative real-time observations of a tidal bore in a macro-tidal estuary are difficult and dangerous, particularly in large estuaries. Mathematical and numerical models have been used to predict tidal bore advances; however, to date, there have been no validations of large-scale flow patterns. A marine radar can provide valuable real-time information on tidal bore propagation. In this paper, a template matching method using a cross-correlation algorithm was explored to estimate the evolution and celerity of a tidal bore with medium resolution marine radar images. The Qiantang River tidal bore was recorded at two different geographical locations. Characteristic flow patterns were derived and analysed, including temporal changes over a relatively large-scale area. The

experimental results showed that the radar-derived celerity and calculated height of the tidal bore were consistent with visual observations in this estuarine zone.

Keywords: marine radar; tidal bore; field observation; macro-tidal estuary; template matching; bore celerity.

1. Introduction

In an estuarine system, a tidal bore may form at the leading edge of flood tides, propagating upstream during the early flood tide (Tricker, 1965; Wolanski et al., 2004; Chanson, 2012). A tidal bore constitutes hydrodynamic discontinuity in terms of the pressure and velocity fields. Two types of tidal bores may be observed in nature, undular bores and breaking bores, based on their free-surface shapes (Chanson, 2010; Dolgopolova, 2013; Li et al., 2017). The former is characterised by a train of secondary waves following the non-breaking surge front (Peregrine, 1966). The latter presents a sharp discontinuity in free-surface elevation, with a rush and a roar, in the shape of a breaking roller (Lubin et al., 2010; Chanson, 2016). It is estimated that more than 400 estuaries worldwide are affected by tidal bores (Chanson, 2011; Chanson, 2012). Although field observations of tidal bores have been conducted recently (Chanson, 2016; Chanson et al., 2011; Reungoat et al., 2015; Reungoat et al., 2017; Reungoat et al., 2018), there have been relatively few quantitative field studies of large tidal bores.

The Qiantang River tidal bore is a geophysical feature in China (Brownlie, 1901; Dai and Zhou, 1987). This tidal bore has been documented scientifically for nearly 2,000 years (Cartwright, 2000; Krehl, 2009). Pertinent accounts include those of Wang (85), Shi (1252), Moore (1888) and the Whangpoo Conservancy Board (1921) and, more recently, have included those of Zhu (2012), Xie and Pan (2013), Xu et al. (2016) and Chanson (2016). Figure 1 presents the Qiantang River estuary. This estuary is a macro-tidal estuary with a funnel shape; its width decreases from the mouth in an upstream direction. The Qiantang River tidal bore results from the funnelling of the flood tidal wave into Hangzhou Bay (Chen et al., 1990; Madsen et al., 2005; Fan et al., 2012; Fan et al., 2014). Its upstream propagation takes place at a long distance, exceeding 100 km; numerous tidal bore warning signs have been erected on the river banks because of human deaths due to drowning in the bore (Pan and Chanson, 2015; Reungoat et al., 2018).

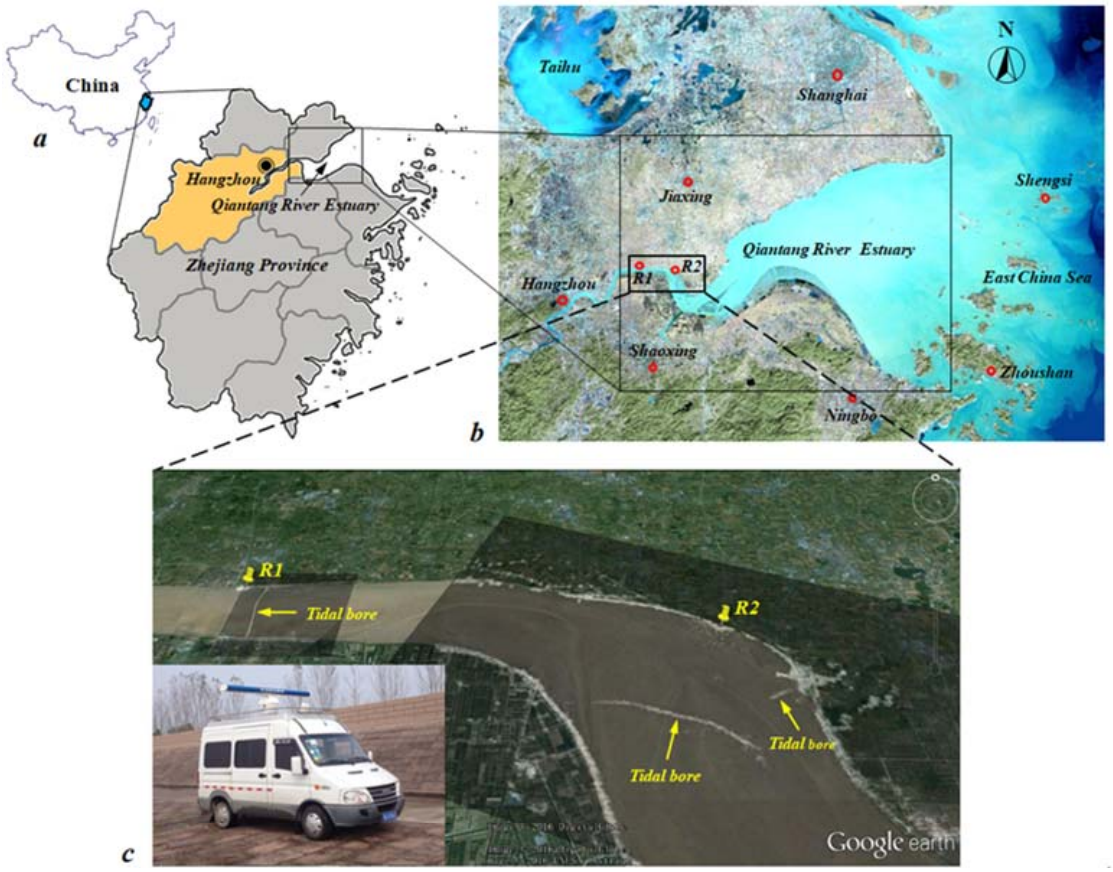

Figure 1. Details of the Qiantang River Estuary, China. (a) Location of the Qiantang River Estuary in China; (b) Two radar test locations in the Qiantang River Estuary; (c) Test sites of R1-Yanguan and R2-Linhaicun, inset: radar vehicle.

In recent years, marine radar technology has been widely used as a remote sensing tool for monitoring ships and sea conditions in coastal areas (Bell, 1999; Marmorino et al., 2004; Bell and Osler, 2011; Kokkini et al., 2017; Zervakis et al., 2017). Observations of internal waves using radar have been undertaken in the South China Sea (Huang et al., 2016; Zhang et al., 2016), but no studies of tidal bores based on marine radar have been published. We report herein on the propagation of the Qiantang River tidal bore, recorded by marine radar. This study develops a method to quantify the propagation of the tidal bore using medium resolution radar images. Following the introduction in Section 1, the data capture system and the image matching by cross-correlation are described in Section 2. The results concerning the evolution and celerity of the tidal bore are presented in Section 3. A discussion and summary of the results are presented in Sections 4 and 5, respectively.

2. Materials and Methods

2.1. Radar data capture system

The radar data was collected with a system located at Yanguan (R1 in Figure 1c, 30°24'08.55"N and 120°33'07.08"E) and Linhaicun (R2 in Figure 1c, 30°22'59.77"N and 120°43'21.11"E) in the Qiantang River Estuary. A 6.5 foot (2.04 m) long radar antenna was mounted on the roof of a

non-moving vehicle (see inset of Figure 1c) and radar data acquisition tools were installed inside the vehicle. The system was base on a Furuno FAR-2127 marine radar employing 25-kW peak-power magnetron transmitters producing a beam width of 1.23° in a horizontal and 20° of a vertical plane, resulting in a range resolution of approximate 10 m over the scanned area with radius of 5 km. The antenna rotated at 42 rotations per minute (rpm), providing a revisit time of 1.429 s. The field observations were undertaken on 13 November 2015 at R1 with radar scan radius of 5 km and on 14 November 2015 at R2 with radar scan radius of 10 km. Table 1 summarises the operating parameters of the radar.

Table 1. Parameters of the radar system used in the Qiantang River Estuary.

System parameter	Value
Peak output power	25 kW
Antenna type	2040 mm Open (6.5')
Frequency	9410±30 MHz (X-band)
Beam Width (Horizontal)	1.23˚(6.5' Open: XN-20AF)
Beam Width (Vertical)	20˚
Range Scales	0.125 - 96 nm
Antenna Rotation Speed	42 r/min
Temperature	Antenna: -25℃ to + 55℃; others: -15℃ to + 55℃
Waterproofing	Processor unit: IPX0; Antenna unit: IPX6

2.2. Template matching using a cross-correlation algorithm

The data were analysed to determine the celerity (phase velocity) vectors of the front of the tidal bore and to obtain potentially real-time information on the bore propagation. A cross-correlation algorithm was used to estimate spatial displacements (Δx, Δy) during a small increment of time Δt of 5.716 s (4 times the rotation period of radar antenna). Lengthways and transverse celerity magnitudes were calculated as u and v, respectively, as follows:

$$u = \frac{\Delta x}{\Delta t}, \quad v = \frac{\Delta y}{\Delta t}, \tag{1}$$

In the matching algorithm, image-patches of pixels from a set of paired radar images are compared and matched. Figure 2 shows the matching concept and illustrates some commonly used terms, such as the template (T) that is the image-patch as a small portion of a reference image (Figure 2a); the search window refer to the search space within which we are hoping to find out a match to the template in a paired image (Figure 2b); and the subimage (S) is the overlapped area when the template (T) moves in the search window of pixel size $N \times N$. The cross-correlation coefficient

between two image-patches T and S of pixel size $M \times M$ is defined by

$$R(i,j) = \frac{\sum_{m=1}^{M}\sum_{n=1}^{M} S^{i,j}(m,n) \times T(m,n)}{\sqrt{\sum_{m=1}^{M}\sum_{n=1}^{M}[S^{i,j}(m,n)]^2}\sqrt{\sum_{m=1}^{M}\sum_{n=1}^{M}[T(m,n)]^2}} \quad (2)$$

where i, j are the coordinates of the upper left corner in the subimage (S). Among all the computed $R(i,j)$, the one with the largest value shows the cross-correlation coefficient for the best match, and $S_{i,j}$ is the match of T, which has been shifted by Δx in the x direction and by Δy in the y direction. The same procedure is repeated for other template in the reference image. This calculation yielded the bore celerity vector along the bore front in a manner comparable to that of Particle Tracking Velocimetry (PTV) (Fujita et al., 1998; Jodeau et al., 2008; Muste et al., 2008; Aberle et al., 2017).

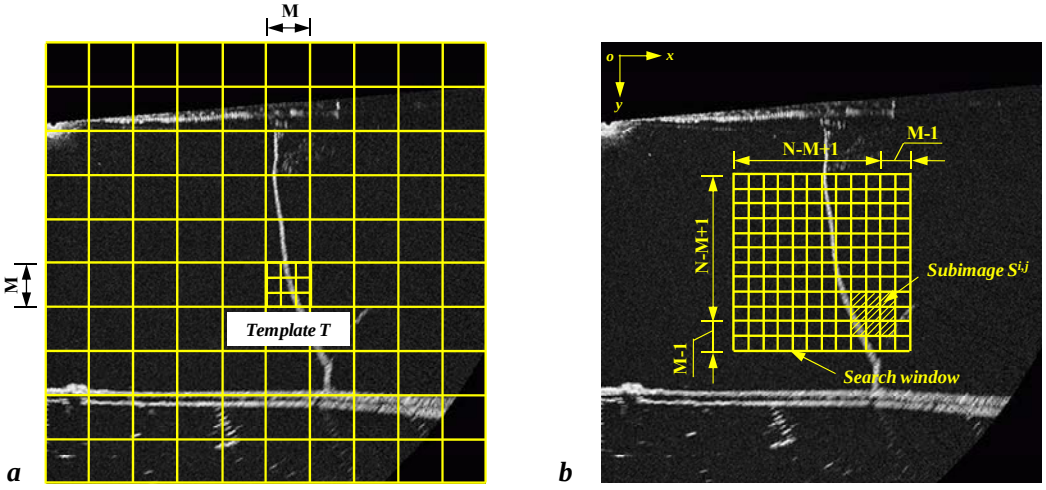

Figure 2. Sketch map of tidal bore radar image template matching concept. (a) Template in a reference radar image; (b) Search window and subimage in a paired radar image.

2.3. Additional hydrodynamic and topographic data

To describe the hydrodynamic conditions of this study area, we considered the records of Yanguan Qiantang Bore Observation Station located 75 m upstream from R1 (see Figure 3). This station has been operating since 2015 and performed recordings of tide level, discharge, current velocity and direction, suspended sediment concentration, pressures induced by the tidal bore on

seawall and pier.

Figure 3. Photos of observation station and tidal bore. (a) Yanguan Qiantang Bore Observation Station; (b) Incoming tidal bore at site R1.

Three regular bathymetry surveys were carried out by the Zhejiang Surveying Institute of Estuary and Coast, China, in March, July and October 2015 (see Figure 4). An echo sounder manufactured by Odom Hydrographic Systems, Inc., USA, was used to measure the water depths and a Real-Time Kinematic Global Positioning Satellite (RTK-GPS) system was employed to determine the locations. The sounding datum refereed to the level of lowest astronomical tide and the elevation used the 1985 National Vertical Datum of China. The survey in October 2015 was closer in time to the in-situ radar observations studied here. The water depth values mentioned later were derived from this survey.

The topographic distributions of sandbars and main channels varied dramatically in between the three surveys. During the flood season from March to July, the scouring of main channel increased and deposition on the sandbar decreased. The main channel widened, while the elevation of sandbars tended to decrease. It was a contrary situation during the dry season from October to March. From July to October, the freshwater runoff weakened gradually and the tidal current increased firstly, reaching a maximum in September and then decreased. The significant difference in range of sandbars and main channels in the surveys emphasises the dynamic characteristics of the bathymetry in this area. This morphodynamic evolution may play an important role in tidal bore propagation and evolution (Chanson 2012). The flow direction of the three main flood currents along the bank are basically marked as A, B and C in Figure 4. The two main currents A and B were firstly separated by central sandbar then converged on the upstream side of R2, formed a single main current C and advanced forward.

LI, Y., PAN, D.Z., CHANSON, H., and PAN, C.H. (2019). "Real-Time Characteristics of Tidal Bore Propagation in the Qiantang River Estuary, China, Recorded by Marine Radar." *Continental Shelf Research*, Vol. 180, pp. 48-58 (DOI: 10.1016/j.csr.2019.04.012) (ISSN 0278-4343).

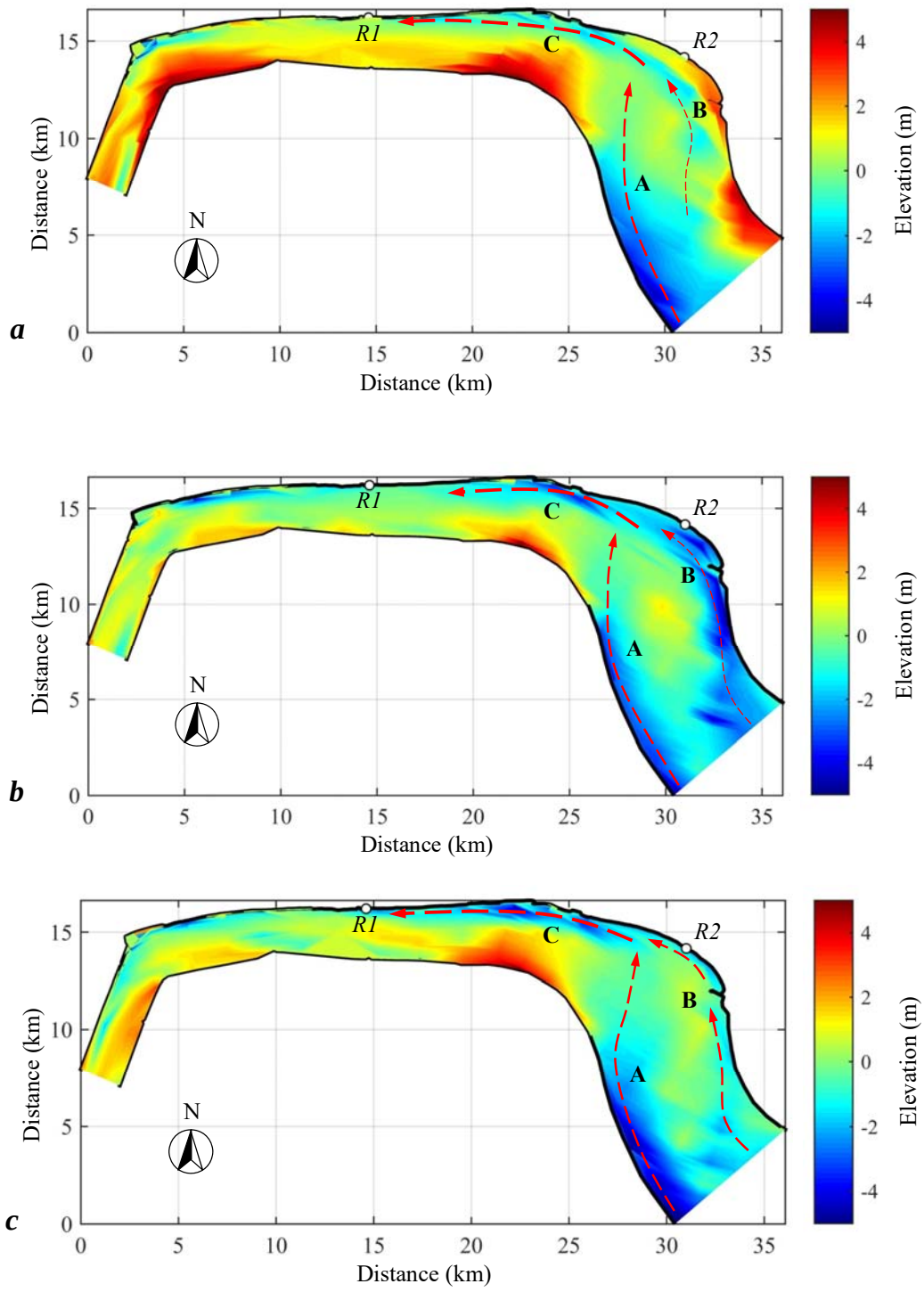

Figure 4. Survey data in (a) April 2015, (b) July 2015 and (c) November 2015, showing the significant changes of bathymetry in the study area. Red dashed arrows basically represent the flood tidal flow direction of the three main currents along the bank.

3. Results

3.1. River Conditions

The tidal bore was observed at two different locations (Figure 1c), Yanguan (R1) and Linhaicun (R2), where the bore shape and pattern were substantially different. At Yanguan (R1), the bore is called the "Silk Bore" because the shape of the leading front looks similar to a silk thread. At Yanguan, the main channel of the river leans close to the north bank, and the width of the river is approximately 2.7 km. Before the arrival of the tidal bore on 13 November 2015, the mean water depth was 1.8 m, the average river flow velocity at the surface was 2.0 m/s, and the average height of the tidal bore was 1.4 m.

Linhaicun (R2) is a location where the two branches of the tidal bore meet, i.e., a "tidal bore crossing", and where the northern seawall is affected by large loads during bore impact. This bore encounter is called the "Crossing Bore". In the measurement area, the mean width of the river was 6.8 km. Before the bore arrival on 14 November 2015, the mean water depth was 1.6 m, and the average flow velocity at the surface was 1.0 m/s, while the average height of the tidal bore was 1.3 m. The mean water depth, the average flow velocity and the height of the tidal bore at the channel near the south bank were larger than those at the channel near the north bank.

3.2. Evolution of the tidal bore

The analysis of the tidal bore evolution was based upon the measurements of the positions of bore front for each radar image. The first step in detecting the bore front was to convert RGB (Red, Green, and Blue) images to grayscale by eliminating the hue and saturation information while retaining the luminance. Then, a reference image without tidal bore (Figure 5a and 5b) was subtracted from each paired image to form a differential image. These difference images (Figure 5c and 5d) separated tidal bore propagation from other bright but unchanged pixels, such as seawall, groyne and channel bank. Next, an algorithm was developed to detect the significant bright points though a thresholding operation and finally a line of best fit with these points can be determined as the front trajectory of tidal bore by the method of least squares.

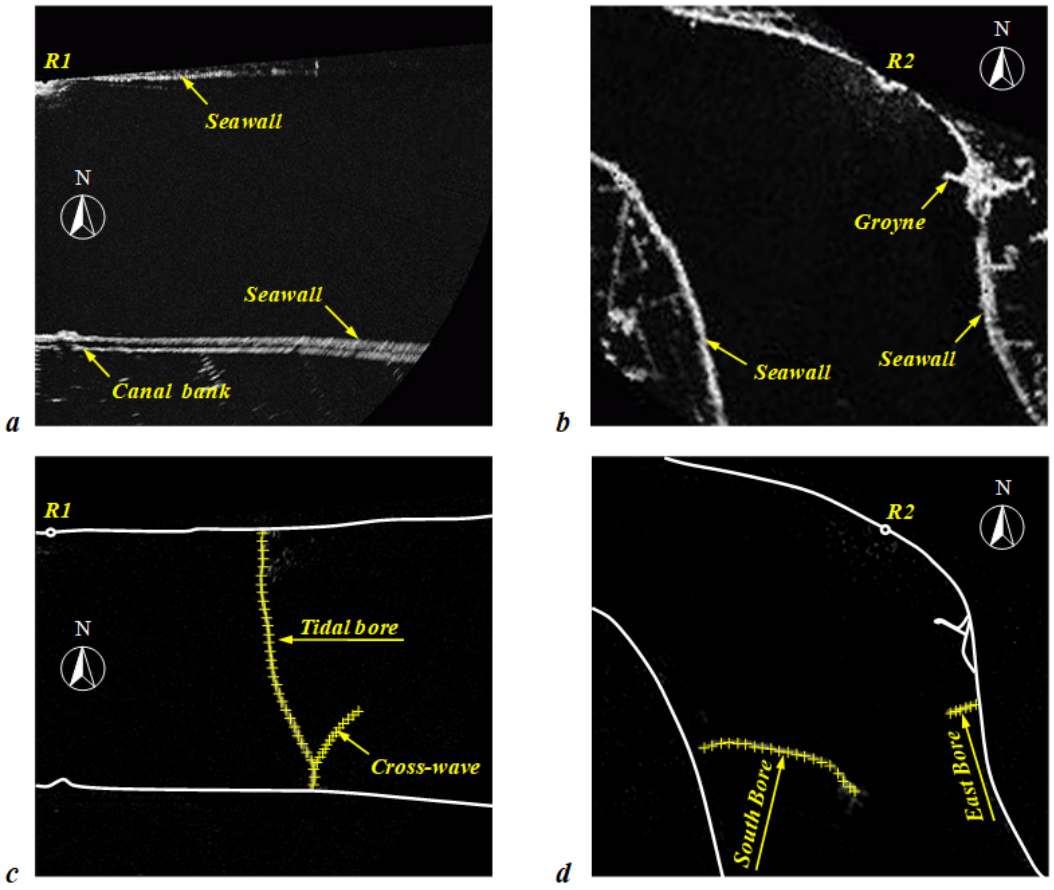

Figure 5. Front trajectories of tidal bore detecting concept. A reference image without tidal bore (a) at R1 and (b) at R2. A differential image (c) at R1 and (d) at R2. Yellow cross points represent detected bright points. A line of best fit with these points can be determined as the front trajectory of tidal bore.

Based upon the radar images, the front of the tidal bore propagating at Yanguan (R1) is shown in Figure 6a. In the deep channel near the northern bank (depicted at the top of Figure 6a), the front of the tidal bore was nearly perpendicular to the isobaths. In the shoal area, the intersection angles between the front of the tidal bore and the isobaths decreased with decreasing water depth. With the transverse variation in bathymetry linked to the deep channel, an *S*-shaped bore front curve was seen (Figure 6b). Cross-waves were observed at locations where the bore front shape sharply changed (Figure 6c). The cross-waves are shown in Figure 6a with green lines.

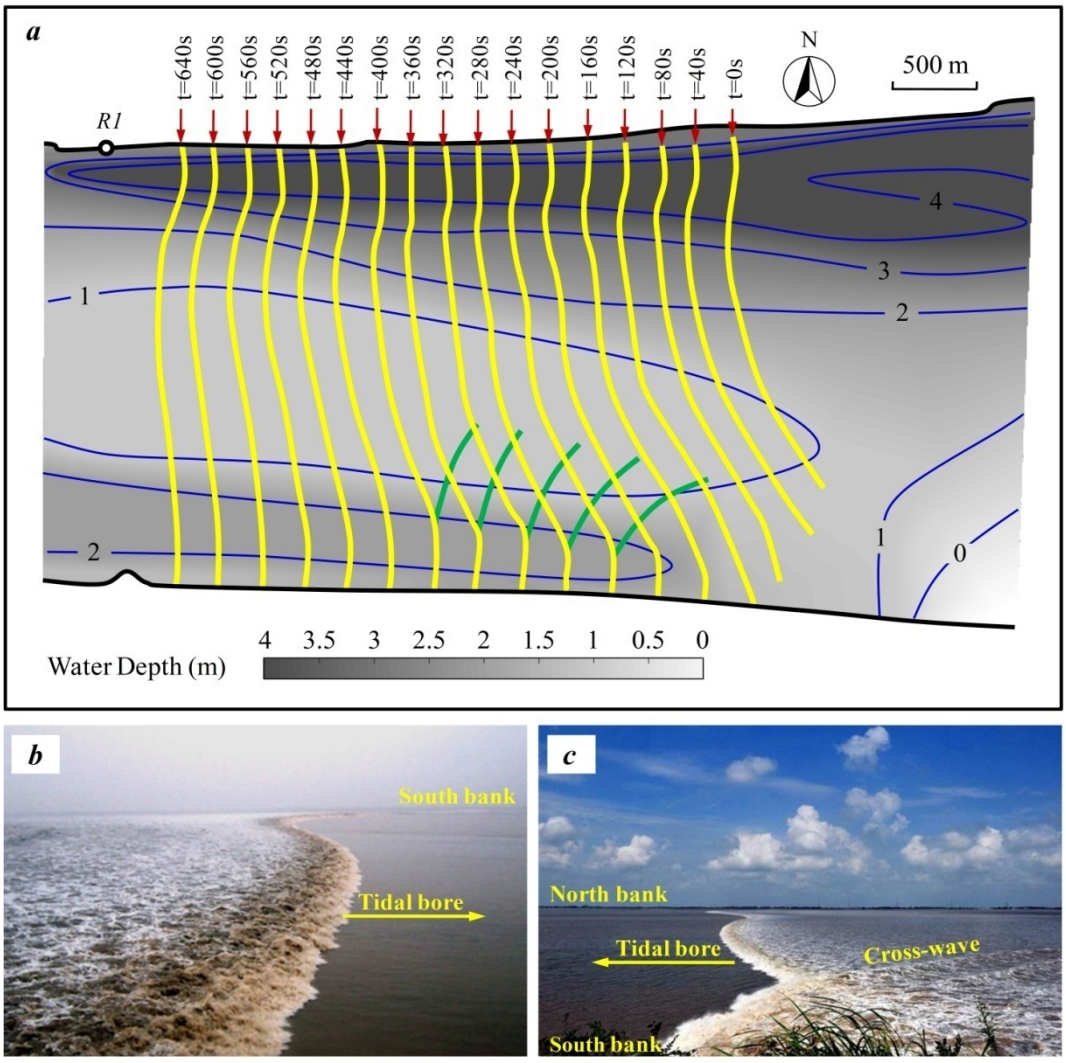

Figure 6. Tidal bore propagation at Yanguan (R1) on 13 November 2015. (a) The front (in yellow) of the tidal bore propagating at Yanguan detailing water depth (in grey-scale map with blue isobaths). The development of cross-waves (in green) observed at the location where the shape of the front sharply changed. (b) Tidal bore observed at the seawall of Yanguan. (c) Tidal bore observed at the opposite bank of Yanguan.

Based on the radar image analyses, the time-evolution of the tidal bore front at Linhaicun (R2) is presented in Figure 7a. The two branches of the tidal bore advanced in different directions linked to varying river channel alignment. The bore front is marked in yellow and green in Figure 7a. One bore, called the South Bore, propagated from south to north (Figure 7b). Another bore, called the East Bore, propagated along the northern bank from east to west (Figure 7c). Later, the two branches of the bore met next to the northern bank, i.e., the Crossing Bore (Figure 7d). Finally, the South Bore impacted on the northern seawall, splashing over the seawall with waters rising as high as 10 m (Figure 7e). In the deep channels near the banks, the fronts of the South and East Bores were also nearly perpendicular to the isobaths (Figure 7a). The front of the South Bore was shaped in a corrugated pattern. In contrast, the front curves of the East Bore were relatively shorter and straighter than those of the South Bore. Figure 7f illustrates a sequence of tidal bore fronts retrieved from marine radar

data in 5-marine radar image intervals from t = 1200 s to t = 1300 s. They show that the two bores first encountered at t = 1221 s. After that, the East Bore became weak and gradually ceased to be observable. From the medium resolution radar images with a resolution of 20 m, the whole encounter process lasted for more than a minute.

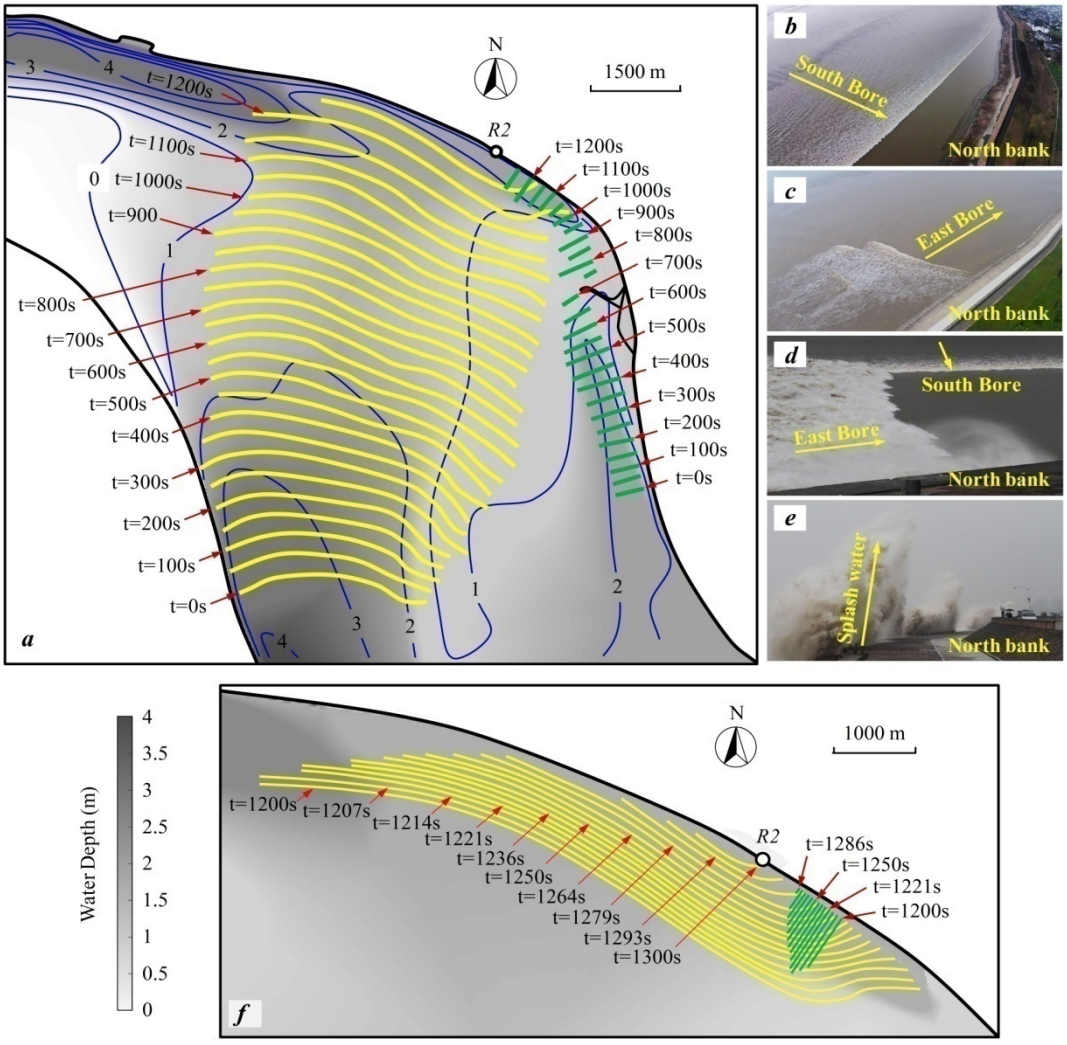

Figure 7. Tidal bore propagation at Linhaicun (R2) on 14 November 2015. (a) Two branches of tidal bores propagating at Linhaicun (water depth in grey-scale map with blue isobaths). The front is illustrated in yellow (the South Bore) from south to north; the green (the East Bore) propagating along the bank from east to west; two branches of the tidal bore encountered near the north bank (the Cross Bore). (b) South Bore propagation from south to north. (c) East Bore propagation from east to west. (d) Cross Bore near the north bank. (e) South Bore splashed over the bank with water rising higher than 10 m. (f) The two-bore encounter observed from radar data in 5-marine radar image intervals during a 100-second period.

3.3. Celerity of the tidal bore

A key feature of a tidal bore is its celerity or propagation speed. While the mean celerity may be derived analytically for simplistic boundary conditions (Tricker, 1965; Peregrine, 1966; Chanson, 2011), both field and laboratory observations have shown that the bore celerity fluctuates rapidly with time and space, even in simple geometry (Leng and Chanson, 2015a, Wang et al., 2017). Calculations in complex natural systems are far from trivial (Chanson, 2012), especially for accurate predictions and early warning. However, the rapid time and spatial fluctuations are rarely taken into consideration (Leng and Chanson, 2015b).

The results of the tidal bore celerity analysis at Yanguan (R1) are presented in Figure 8a. In Figure 8a, the black and blue arrows represent the fronts and cross-waves of the tidal bore, respectively. Neglecting local sharp fluctuations, the main tidal bore celerity contours are shown in 0.3 m/s intervals. Overall, the tidal bore celerity ranged between 5.4 m/s and 7.3 m/s, with a mean value of approximately 6.1 m/s. The cross-wave celerity spanned between 6.4 m/s and 8.2 m/s, with a mean celerity of 7.5 m/s. The celerity of the tidal bore was faster along the southern bank than that along the northern bank. In fact, the average celerity along the northern bank was 5.2 m/s, and the average celerity along the southern bank was 6.5 m/s.

Figure 8b shows the data in terms of the tidal bore celerity at Linhaicun (R2). In Figure 8b, the black and blue arrows represent the fronts of the South Bore and the East Bore, respectively. The main celerity contours are presented in 0.6 m/s intervals. Overall, the South Bore propagated faster than the East Bore. The South Bore celerity was between 5.1 m/s and 8.2 m/s, with a mean value of 6.9 m/s. The East Bore celerity ranged between 4.6 m/s and 5.5 m/s, with a mean of approximately 5.0 m/s. Variation in both celerity magnitude and direction might be due to the locally varying bottom topography.

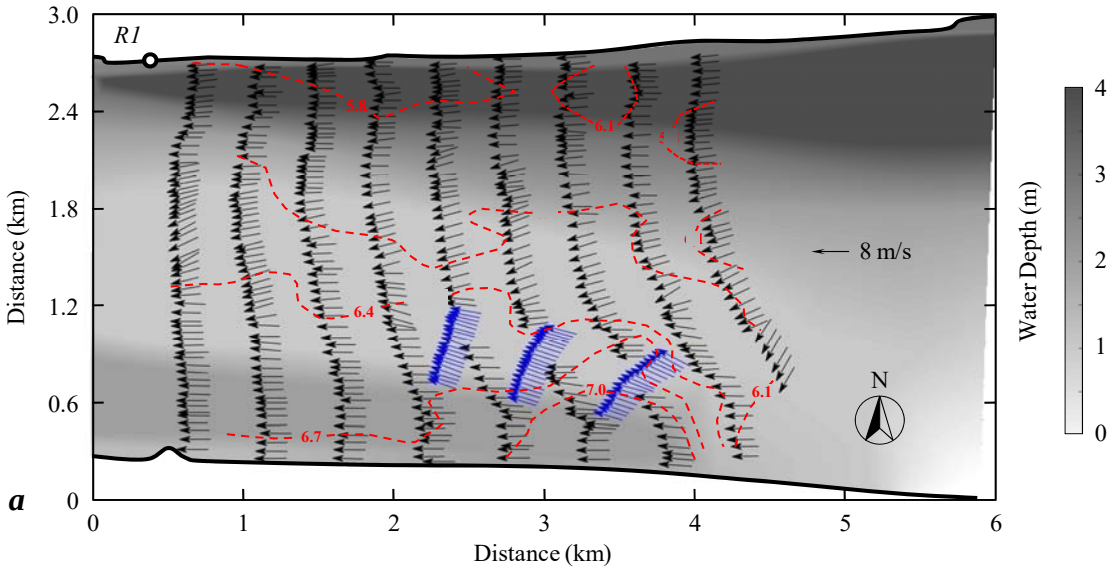

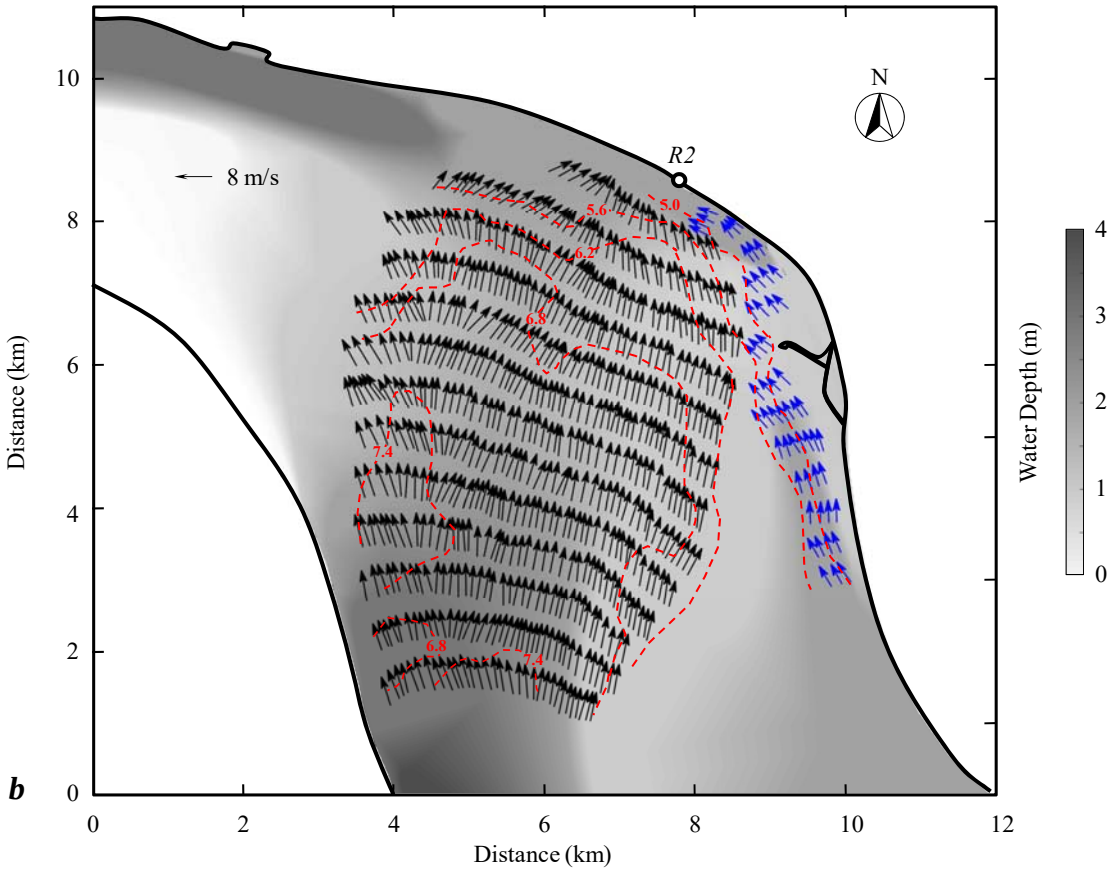

Figure 8. Tidal bore front celerity data and water depth (in grey-scale map). (a) Celerity (phase velocity) vectors (in black) of the tidal bore propagating at Yanguan (R1). The arrows refer to the direction of celerity. Blue arrows show the cross-wave celerity vectors. The celerity contours (dashed lines in red) are at 0.3 m/s intervals. (b) Celerity (phase velocity) vectors of the tidal bore propagating at Linhaicun (R2). The arrows refer to the direction of celerity. Blue arrows show the East Bore celerity vectors. Black arrows show the South Bore celerity vectors. The celerity contours (dashed lines in red) are at 0.6 m/s intervals.

4. Discussion

4.1. Comparison with visual observations

This study used radar images to derive the time evolution of free-surface flow patterns of a large tidal bore, delivering a large-scale view in a macro-tidal estuary. For safety, a security video monitoring system, called Mega Eyes (Figure 9a), has been installed on the seawall of Qiantang River. The installation locations are shown in Figure 9d for the study area. This mature technology has been used to visually observe tidal bores in Qiantang River Estuary for over 10 years. The arrival time and height of the tidal bore were interpreted based on these observations combined with water gauge data (Figure 9f).

The comparative results between visual observations and radar-derived outcomes are shown in Table 2. The average celerity of the tidal bore from Xilongtou to R1 on 13 November 2015 was 5.3 m/s. This result was very similar to the radar-derived average celerity along the northern bank, near

R1, of 5.2 m/s. The average celerity of the tidal bore from R2 to Xincang on 14 November 2015 was 5.5 m/s. The radar-derived average celerity along the northern bank, near R2, was 5.0 m/s.

Although there were few data compared with visual observations, the feasibility and accuracy of the tidal bore information derived from marine radar image sequences, as a relatively novel technology, were in relatively good agreement with the visual observations extracted from the Mega Eyes system.

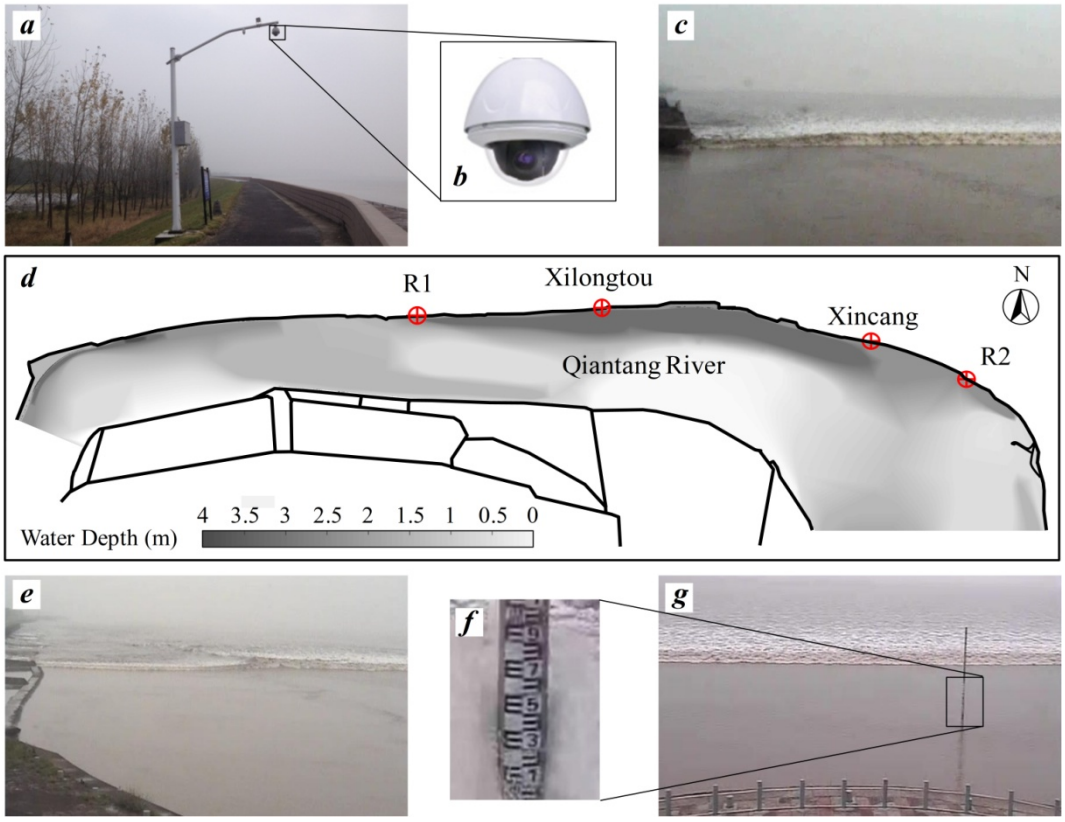

Figure 9. Field observations with the Mega Eyes system. (a) Mega Eyes system; (b) camera; (c) Yanguan (R1); (d) Location diagram and water depth (in grey-scale map). (e) Xilongtou; (f) water gauge; (g) Xincang.

Table 2a. Comparison between visual observations and radar-derived outcomes on 13 November 2015.

Location	Arrive time (h: min: s)	Height (VO) (m)	Height (RD) (m)	Distance (m)	Celerity* (VO) (m/s)	Celerity$^{\#}$ (RD) (m/s)
Linhaicun (R2)	11:58:09	1.2	-	3050	5.8	-
Xincang	12:06:54	1.5	-			
Xilongtou	12:26:44	1.2	1.1	5870	5.3	5.2
Yanguan (R1)	12:45:16	1.4	1.2			

VO: visual observations; RD: Radar-derived; Celerity*: equal to the distance travelled divided by the time; Celerity$^{\#}$: radar-derived average value along the bank.

Table 2b. Comparison between visual observations and radar-derived outcomes on 14 November 2015.

Location	Arrive time (h: min: s)	Height (VO) (m)	Height (RD) (m)	Distance (m)	Celerity* (VO) (m/s)	Celerity# (RD) (m/s)
Linhaicun (R2)	12:27:16	1.3	1.1	3050	5.5	5.0
Xincang	12:36:32	1.6	1.3			
Xilongtou	12:56:49	1.0	-	5870	5.4	-
Yanguan (R1)	13:15:06	1.5	-			

VO: visual observations; RD: Radar-derived; Celerity*: equal to the distance travelled divided by the time; Celerity#: radar-derived average value along the bank.

4.2. Approximate calculation of the tidal bore height

Considering tidal bore progression through an estuary, the motion of the bore front can be analysed as a quasi-steady hydraulic jump in translation, travelling from a downstream to an upstream direction with celerity C (Figure 10). The integral forms of the mass and momentum conservation equations provide a series of relationships between the flow properties preceding and following the bore front (Chanson, 2011):

$$(V_1 + C)d_1 = (V_2 + C)d_2 \quad (3)$$

$$\frac{1}{2}\rho g(d_2^2 - d_1^2) = \rho(V_1 + C)d_1(V_1 - V_2) \quad (4)$$

where V is the cross-sectional average flow velocity, d is the water depth, ρ is the water density, g is the gravity acceleration, and the subscripts 1 and 2 refer to the flow conditions at sections 1 and 2, i.e., before and immediately after the bore front. The solution to equations (3) and (4) yields the height of the tidal bore H:

$$H = \frac{d_1}{2}\left(\sqrt{1 + 8Fr^2} - 3\right) \quad (5)$$

with the bore Froude number Fr defined as:

$$Fr = \frac{V_1 + C}{\sqrt{gd_1}} \quad (6)$$

and $H = d_2$-d_1.

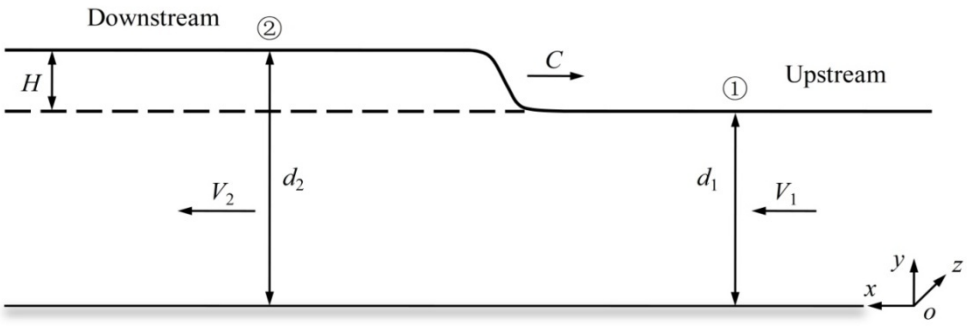

Figure 10. Definition sketch of a tidal bore propagating upstream.

The Qiantang River tidal bore celerity C ranged from 4 to 10 m/s, which is 5 to 10 times larger than the initial cross-sectional average flow velocity V_1 in the first approximation, $V_1 = Q_1/A_1$, where Q_1 is the freshwater runoff and A_1 is the initial flow cross-section area. We used the records of Yanguan Qiantang Bore Observation Station and the bathymetric survey of in October 2015. The estimated initial cross-sectional average flow velocity was 0.6 to 0.8 times the flow velocity at the surface. The initial cross-sectional average flow velocity near R1 and R2 were 1.2 m/s and 0.6 m/s, respectively.

Based on the bathymetric survey of the estuary, the height of the bore was estimated from Equation (5) using the observed water depth, the bore celerity derived from the marine radar images and the initial cross-sectional average flow velocity. Figure 11 presents the bore height H results along the investigated areas. Although no quantitative direct comparison with in-situ data was available over such a large-scale area, the magnitude and trends of the tidal bore height at the two sites were consistent with those expected from both visual observations (Table 2) and depth-averaged numerical calculations (Pan et al., 2007; Pan and Huang, 2010; Wang and Pan, 2018) for these estuarine areas. The data suggested that the tidal bore height tended to decrease with increasing water depth in the main channel near the bank of the Qiantang River. In the shoaling area, the tidal bore height, to some extent, increased with decreasing water depth. Additional research is necessary to provide a conclusive explanation for this phenomenon.

LI, Y., PAN, D.Z., CHANSON, H., and PAN, C.H. (2019). "Real-Time Characteristics of Tidal Bore Propagation in the Qiantang River Estuary, China, Recorded by Marine Radar." *Continental Shelf Research*, Vol. 180, pp. 48-58 (DOI: 10.1016/j.csr.2019.04.012) (ISSN 0278-4343).

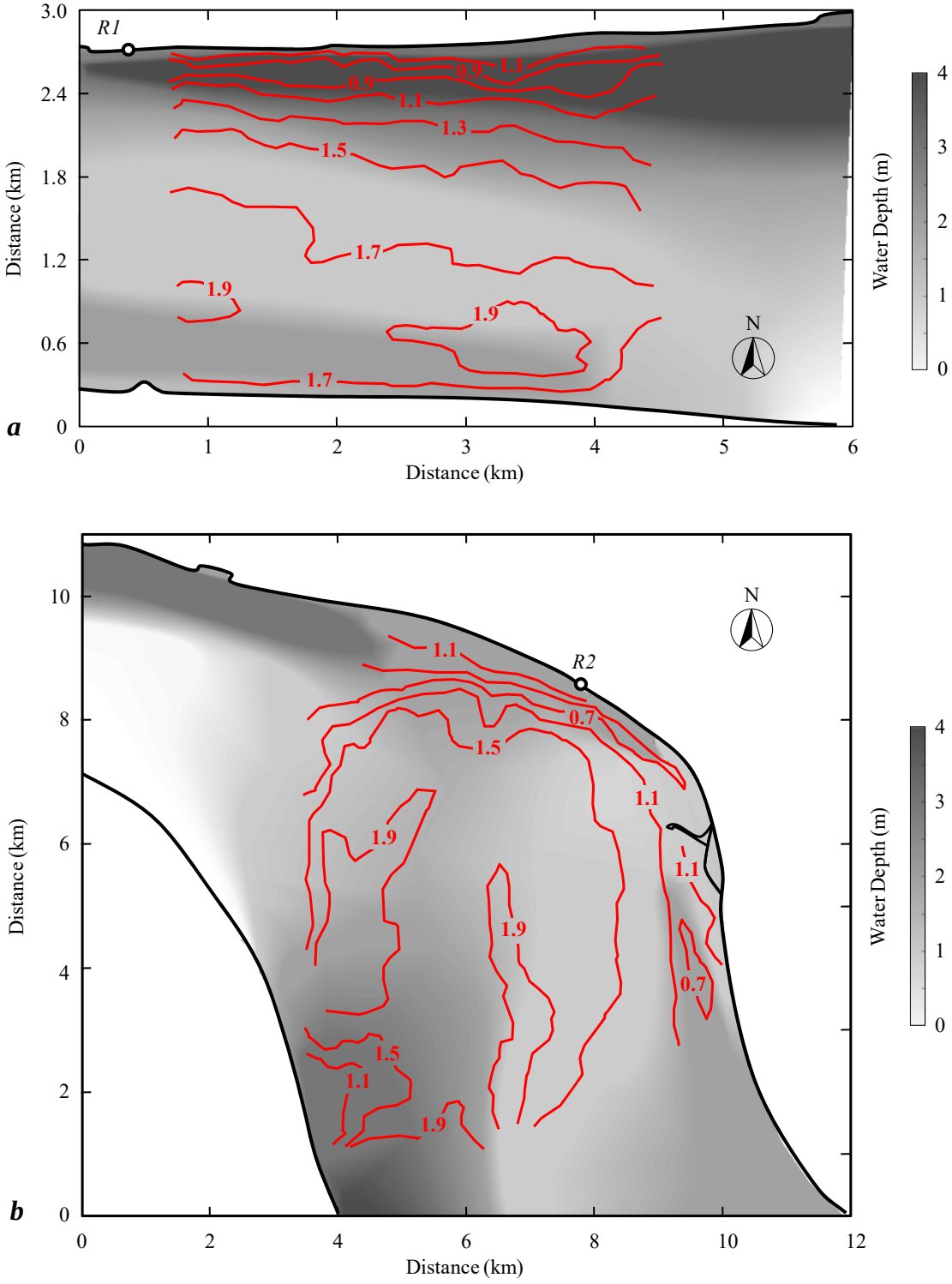

Figure 11. Contour plot of estimated tidal bore height (Units: m) and water depth (in grey-scale map). (a) Yanguan (R1); (b) Linhaicun (R2).

4.3. Errors from the performed analyses and application perspective

During the observation period, the minimum celerity of tidal bore in the study area was approximately 5 m/s. The resolution of radar images obtained at R1 and R2 is 10 m and 20 m respectively. Considering the accuracy requirement of analysis, the time interval of a set of paired images used for matching at R1 and R2 should be greater than 2 s and 4 s respectively. In the current study, a time interval of 4 times the rotation period of radar antenna, i.e., 5.716 s, was selected as described in Subsection 2.2. Thus, the small celerity features during this time interval are smoothed. The limitation of this analysis need to be fully studied and it may relate to the resolution of the radar images. Further works should examine the exact correspondence between radar image-derived celerity and other direct instrumented measurements.

In Section 4.2, it was shown that the water depth (bathymetry), bore height and celerity are interrelated in a first approximation. The bathymetry is very difficult to obtain, at a reasonable price, and is rarely done on a regular basis. Meanwhile, the estuary water surface could provide the raw data about bore height and celerity. Although the measurement of bore height is much more difficult to obtain over a large area, it is perhaps achievable with photogrammetry or radar in selected locations. Consequently, the water bathymetry could be potentially derived from the celerity and height of the tidal bore in an inverse analysis based on hydrodynamic analysis of a macro-tidal estuary, as is the case in wave field analysis (Bell, 1999).

5. Conclusions

Marine radar image sequences were recorded, processed and analysed to determine the evolution and celerity of a very-large tidal bore in a macro-tidal estuary. The results demonstrated that the radar-derived celerity and height of the tidal bore were consistent with visual observations. The radar-image data delivered further detailed insights into the temporal evolution of the tidal bore, including spatial variations, which to date have been rarely documented, while providing real-time data that could be used to ensure the safety of tidal bore watchers.

Further research should include the following topics: (1) the feasibility of the radar method in comparison with field results using other direct instruments and measurements; (2) a more efficient matching algorithm with high resolution radar images to improve the accuracy of inversion; (3) shallow water bathymetry estimates based on hydrodynamic analysis of a macro-tidal estuary. Further, quantitative real-time observations of large-scale hydrodynamic events such as tsunami spread and run-up, flood waves resulting from dam break, spillway gate malfunction and landslide are a challenging problem in terms of instrument application and direct measurements. The presented method based upon radar image analysis would seem to provide a useful technique to estimate characteristic flow patterns in real time during such natural disaster events.

Acknowledgements

This work was supported by the National Natural Science Foundation of China [grant numbers 41876095, 51779228 and 50809062]; Zhejiang Provincial Natural Science Foundation of China [grant number Y5110076]; China Scholarship Council and Zhejiang Association for International Exchange of Personnel.

References

1. Aberle, J.; Rennie, C., Admiraal, D.M., Muste, M. *Experimental Hydraulics: Methods, Instrumentation, Data Processing and Management. Vol. II. Instrumentation and Measurement Techniques*. IAHR Monograph, Taylor and Francis: New York NY, USA, 2017.
2. Bell, P.S. Shallow water bathymetry derived from an analysis of X-band marine radar images of waves. *Coastal Engineering*, 1999, 37, 513–527, doi:10.1016/S0378-3839(99)00041-1.
3. Bell, P.S.; Osler, J.C. Mapping bathymetry using X-band marine radar data recorded from a moving vessel. *Ocean Dynamics*, 2011, 61, 2141–2156, doi:10.1007/s10236-011-0478-4.
4. Brownlie, A. The solution of the problem of the tidal bore. *Bulletin of the American Geographical Society*, 1901, 33, 318–324.
5. Cartwright, D.E. *Tides: A scientific History*. Cambridge University Press: Cambridge, England, 2000.
6. Chanson, H. Atmospheric Noise of a Breaking Tidal Bore. *Journal of the Acoustical Society of America*, 2016, 139(1), 12–20, doi:10.1121/1.4939113.
7. Chanson, H. Current knowledge in tidal bores and their environmental, ecological and cultural impacts. *Environmental Fluid Mechanics*, 2011, 11, 77–98, doi:10.1007/s10652-009-9160-5.
8. Chanson, H. *Tidal bores, Aegir, Eagre, Mascaret, Pororoca: Theory and observations*. World Scientific: Singapore, 2012.
9. Chanson, H. Undular Tidal Bores: Basic Theory and Free-surface Characteristics. *Journal of Hydraulic Engineering*, 2010, 136(11), 940–944, doi:10.1061/(ASCE)HY.1943-7900.0000264.
10. Chanson, H.; Reungoat, D.; Simon, B; Lubin, P. High-frequency turbulence and suspended sediment concentration measurements in the Garonne River tidal bore. *Estuarine, Coastal and Shelf Science*, 2011, 95, 298–306, doi:10.1016/j.ecss.2011.09.012.
11. Chen, J.; Liu, C.; Zhang, C.; Walker, H.J. Geomorphological development and sedimentation in the Qiantang Estuary and Hangzhou Bay. *Journal of Coastal Research*, 1990, 6, 559–572.
12. Dai, Z.-H.; Zhou, C.-S. The Qiantang Bore. *International Journal of Sediment Research*, 1987, 1, 125–133.
13. Dolgopolova, E.N. The conditions for tidal bore formation and its effect on the transport of saline water at river mouths. *Water Resources*, 2013, 40, 16–30, doi:10.1134/S0097807813010028.
14. Fan, D.; Cai, G.; Shang, S.; Wu, Y.; Zhang, Y.; Gao, L. Sedimentation processes and sedimentary characteristics of tidal bores along the north bank of the Qiantang Estuary. *Chinese Science Bulletin*, 2012, 57, 1157–1167, doi:10.1007/s11434-012-4993-6.
15. Fan, D.; Tu, J.; Shang, S.; Cai, G. Characteristics of tidal-bore deposits and facies associations in the Qiantang Estuary, China. *Marine Geology*, 2014, 348, 1–14, doi:10.1016/j.margeo.2013.11.012.
16. Fujita, I.; Muste, M.; Kruger, A. Large-scale particle image velocimetry for flow analysis in hydraulic engineering applications. *Journal of Hydraulic Research*, 1998, 36, 397–414, doi:10.1080/00221689809498626.
17. Huang, X.; Chen, Z.; Zhao, W.; Zhang, Z.; Zhou, C.; Yang, Q.; Tian, J. An extreme internal solitary wave event observed in the northern South China Sea. *Scientific Reports*, 2016, 6, 30041, doi:10.1038/srep30041.
18. Jodeau, M.; Hauet, A.; Paquier, A.; Le Coz, J.; Dramais, G. Application and evaluation of LS-PIV technique for the monitoring of river surface velocities in high flow conditions. *Flow Measurement and Instrumentation*, 2008, 19, 117–127, doi:10.1016/j.flowmeasinst.2007.11.004.
19. Kokkini, A.; Zervakis, V.; Mamoutos, I.; Potiris, E.; Frangoulis, C.; Kioroglou, S.; Maderich, V.; Psarra, S. Quantification of the surface mixed-layer lateral transports via the use of a HF radar:

Application in the North-East Aegean Sea. *Continental Shelf Research*, 2017, 149, 17–31, doi:10.1016/j.csr.2017.04.006.

20. Krehl, P.O.K. *History of Shock Waves, Explosions and Impact: A Chronological and Biographical Reference*. Springer-Verlag: Berlin, Germany, 2009.
21. Leng, X.; Chanson, H. Turbulent advances of a breaking bore: preliminary physical experiments. *Experimental Thermal and Fluid Science*, 2015a, 62, 70–77, doi:10.1016/j.expthermflusci.2014.12.002.
22. Leng, X.; Chanson, H. Breaking Bore: Physical Observations of Roller Characteristics. *Mechanics Research Communications*, 2015b, 65, 24–29, doi:10.1016/j.mechrescom.2015.02.008.
23. Li, Y.; Pan, D.-Z.; Chanson, H.; Pan, C.-H. Tidal bore progressing on a small slope. *Experimental Thermal and Fluid Science*, 2017, 88, 513–518, doi:10.1016/j.expthermflusci.2017.07.004.
24. Lubin, P.; Glockner, S.; Chanson, H. Numerical simulation of a weak breaking tidal bore. *Mechanics Research Communications*, 2010, 37, 119–121, doi:10.1016/j.mechrescom.2009.09.008.
25. Madsen, P.A.; Simonsen, H.J.; Pan, C.-H. Numerical simulation of tidal bores and hydraulic jumps. *Coastal Engineering*, 2005, 52, 409–433, doi:10.1016/j.coastaleng.2004.12.007.
26. Marmorino, G.O.; Cooper, A.L.; Mied, R.P.; Lindemann, G.J.; Trizna, D.B.; Porter, D.L. Onshore propagation of a buoyant ocean front observed using a shore-based marine radar. *Continental Shelf Research*, 2004, 24, 951–964, doi:10.1016/j.csr.2004.03.011.
27. Moore, R.N. *Report on the Bore of the Tsien-Tang Kiang*. Hydrographic Office: London, UK, 1888, 7–37.
28. Muste, M.; Fujita, I.; Hauet, A. Large-scale particle image velocimetry for measurements in riverine environments. *Water Resources Research*, 2008, 44, W00D19, doi:10.1029/2008WR006950.
29. Pan, C.-H., Lin, B.-Y., Mao, X.-Z. Case study: Numerical modeling of the tidal bore on the Qiantang river, China. *Journal of Hydraulic Engineering*, 2007, 133(2), 130–138, doi:10.1061/(ASCE)0733-9429(2007)133:2(130).
30. Pan, C. H., Huang, W. R. Numerical modeling of suspended sediment transport affected by tidal bore in Qiantang estuary. *Journal of Coastal Research*, 2010, 26(6), 1123–1132, doi:10.2112/JCOASTRES-D-09-00024.1.
31. Pan, D.-Z.; Chanson, H. Physical modelling of tidal bore dyke overtopping: implication on individuals' safety. 2015, Proceedings 36th IAHR World Congress, The Hague, The Netherlands, 27 June-3 July, Theme 4, 3824–3831.
32. Peregrine, D.H. Calculations of the development of an undular bore. *Journal of Fluid Mechanics*, 1966, 25, 321–330.
33. Reungoat, D., Leng, X., Chanson, H. Successive impact of tidal bores on sedimentary processes: Arcins channel, Garonne River. *Estuarine, Coastal and Shelf Science*, 2017, 188, 163–173, doi:10.1016/j.ecss.2017.02.025.
34. Reungoat, D.; Chanson, H.; Keevil, C.E. Field measurements of unsteady turbulence in a tidal bore: the Garonne River in October 2013. *Journal of Hydraulic Research*, 2015, 53, 291–301, doi:10.1080/00221686.2015.1021717.
35. Reungoat, D.; Lubin, P.; Leng, X.; Chanson, H. Tidal Bore Hydrodynamics and Sediment Processes: 2010-2016 Field Observations in France. *Coastal Engineering Journal*, 60 (4), 484-498, DOI: 10.1080/21664250.2018.1529265.
36. Shi, E. *Shunyou reign-period records of Hangzhou district*. 1252, 10, 16. (Seen at Hangzhou District Library, China.)
37. Tricker, R.A.R. *Bores, Breakers, Waves and Wakes: An Introduction to the Study of Waves on*

Water. American Elsevier: New York, USA, 1965.
38. Wang, C. Lun-Heng. 85. In *Miscellaneous essays of WANG CH'UNG*; Translated from the Chinese by Forke, A., New York, 1962, 250–251.
39. Wang, H.; Leng, X.; Chanson, H. Bores and Hydraulic Jumps. Environmental and Geophysical Applications. 2017, *Engineering and Computational Mechanics*, Proceedings of the Institution of Civil Engineers, UK, 170 (EM1), 25–42 doi:10.1680/jencm.16.00025.
40. Wang, Q.-S.; Pan, C.-H. Three-dimensional modelling of sediment transport under tidal bores in the Qiantang estuary, China. *Journal of Hydraulic Research*, 2018, 56(5), 662–672, DOI: 10.1080/00221686.2017.1397781.
41. Whangpoo Conservancy Board. *Report on the Hydrology of the Hangchow Bay and the Chien Tang Estuary*. Series I, Report No. 5; Shanghai Harbor Investigation: Shanghai, China, 1921.
42. Wolanski, E.; Williams, D.; Spagnol, S.; Chanson, H. Undular tidal bore dynamics in the Daly Estuary, Northern Australia. *Estuarine, Coastal and Shelf Science*, 2004, 60, 629–636, doi:10.1016/j.ecss.2004.03.001.
43. Xie, D.-F.; Pan, C.-H. A preliminary study of the turbulence features of the tidal bore in the Qiantang River, China. *Journal of Hydrodynamics*, 2013, 25, 903–911, doi:10.1016/S1001-6058(13)60439-4.
44. Xu, C.-J.; Yin, M.; Pan, X.-D. Field test and numerical simulation of tidal bore pressures on sheet-pile groin in Qiantang River. *Marine Georesources & Geotechnology*, 2016, 34, 303–312, doi:10.1080/1064119X.2014.954683.
45. Zervakis, V.; Kokkini, Z.; Potiris, E. Estimating mixed layer depth with the use of a coastal high-frequency radar. *Continental Shelf Research*, 2017, 149: 4–16, doi:10.1016/j.csr.2016.07.008.
46. Zhang, X.; Wang, J.; Sun, L.; Meng J. Study on the amplitude inversion of internal waves at Wenchang area of the South China Sea. *Acta Oceanologica Sinica*, 2016, 35, 14–19, doi:10.1007/s13131-016-0902-1.
47. Zhu, X.-H.; Zhang, C.; Wu, Q.; Kaneko, A.; Fan, X.; L i, B. Measuring discharge in a river with tidal bores by use of the coastal acoustic tomography system. Estuarine, Coastal and Shelf Science, 2012, 104-105, 54–65, doi:10.1016/j.ecss.2012.03.022.